Temperature Dependence of Order, Disorder, and Defects in Laterally Confined Diblock Copolymer Cylinder Monolayers

Matthew R. Hammond,[†] Eric Cochran,[‡] Glenn H. Fredrickson,[†,‡] and Edward J. Kramer*[,†,‡]

Departments of Materials and Chemical Engineering, University of California, Santa Barbara, California 93106

Received March 7, 2005; Revised Manuscript Received May 31, 2005

ABSTRACT: Monolayer arrays of polystyrene−poly(2-vinylpyridine) diblock copolymer cylinders with excellent orientational order and a very low density of dislocations are prepared by cooling slowly from above the bulk order−disorder temperature (ODT) ~212 °C within silicon oxide channels one cylinder spacing a in depth and 2 μm in width. The translational order of this array, however, is short range with a correlation length of ~12a. If such an array is heated to a temperature above the glass transition temperature of the block copolymer (100 °C) but well below the ODT, a finite density of thermally generated dislocations is observed, which leads to a decrease in the translational correlation length and an appearance of quasi-long-range orientational order such that the orientational correlation function $g_2(r)$ decays as a power law, i.e., $g_2(r) \approx (r/a)^{-\eta_2(T)}$. The state of disorder at any given temperature appears to be an equilibrium one since cylinder arrays with similar dislocation densities and correlation functions can be obtained either by heating from the well-ordered state or by cooling slowly directly to the final temperature and holding at that temperature for a sufficient time. Above a temperature of 195 °C, the orientational order becomes short range ($g_2(r)$ decaying exponentially with r), and a large density of disclinations is observed in addition to the dislocations. The cylinder array becomes isotropic above this temperature, which is ~20 °C below the bulk ODT. These results are in qualitative agreement with the theory of Toner and Nelson[1] which describes the thermal generation of disorder and ultimate melting of a two-dimensional smectic.

Introduction

The 10−100 nm length scale of the self-assembling structures formed in block copolymers has driven recent interest in using these materials in inexpensive, large-area, "bottom-up" device fabrication.[2,3] Thin copolymer films have been demonstrated to serve effectively as nanoscale templates for patterned magnetic and electronic devices.[4−6] An obstacle in realizing the full potential of this method has been the lack of tools for gaining control over the long-range ordering and orientation in the copolymer domains. Exerting this control requires (a) introducing a preferred grain orientation and (b) minimizing "lattice" defects. In the case of block copolymer cylinders lying in the film plane, the system studied here, varying degrees of success in these efforts have been achieved by the use of applied electric fields,[7,8] directional crystallization,[9] and the application of shear.[10] In the present work, we employ graphoepitaxy,[11] a combined top-down/bottom-up approach in which shallow channels prepatterned into the substrate guide the copolymer alignment, an approach first used for cylinders by Sundrani and Sibener.[12−14] Harrison et al. have also shown that the edges of long block copolymer islands will also guide cylinder alignment, and these authors have investigated the order as a function of distance from these island edges.[15]

En route to achieving this control over copolymer orientation and defect structures, the often very slow kinetics by which this ordering is achieved must also be carefully considered. Harrison et al. at Princeton have produced several thorough studies of the dynamics of coarsening in block copolymer cylinder monolayers quenched from the disordered (as deposited) state, determining that defect motion and annihilation are of paramount importance.[16,17] Figure 1 summarizes the types of topological defects observed in these systems: dislocations (Figure 1a) and disclinations (Figure 1b).

The topological barriers to coarsening presented by disclinations, in particular, were emphasized. At temperatures high enough above the copolymer glass transition (yet still strongly segregated) the cylinder orientational correlation length, ξ_2, was shown to grow as $\xi_2 \sim t^{1/4}$. Significantly, the same power-law exponent of $^1/_4$ was also observed in the growth of the average spacing between disclinations (measured as the inverse square root of the disclination density).

Further work by the same group showed that extremely long orientational correlation lengths could be achieved by sweeping a thermal gradient over the sample, provided that the gradient starts above the copolymer order−disorder transition (ODT) and ends well below it.[18] However, no correlation was found between the direction of the temperature gradient and the cylinder orientation. In this work, we take a somewhat similar approach, uniformly heating our films to the disordered state and then slowly cooling the sample into the ordered regime. We show that the combination of this simple thermal treatment and the use of prepatterned substrates allows for the rapid creation of highly ordered cylinder arrays.

The reader may wonder, as we did, whether even faster ordering of the monolayer might be achieved by annealing at temperatures just below the order−

† Department of Materials.
‡ Department of Chemical Engineering.
* To whom correspondence should be addressed. E-mail: edkramer@mrl.ucsb.edu.

10.1021/ma050479l CCC: $30.25
Published on Web 07/01/2005

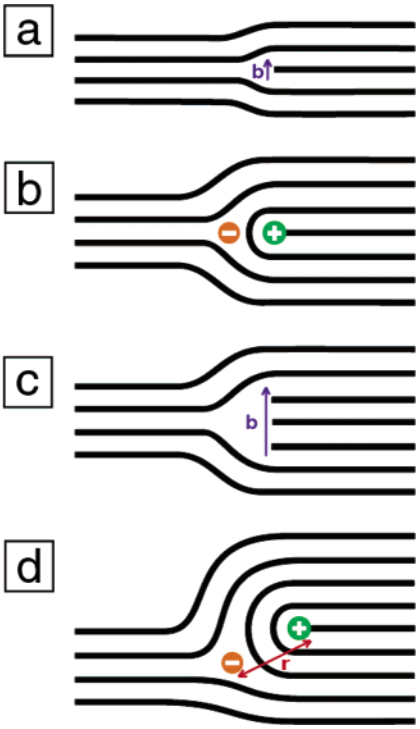

Figure 1. Defect structure schematics in which cylinder cores are represented by the black lines. (a) An elementary dislocation. The Burgers vector **b** is indicated by the blue arrow. (b) A pair of oppositely charged disclinations, each characterized by winding number $s = \pm 1/2$. The $s = -1/2$ disclination is indicated by the orange dot and the $s = +1/2$ disclination by the green dot. Note that a dislocation is composed of a tightly bound pair of disclinations of opposite sign. (c) The disclination pair shown in (b) can be thought of as causing a long-range strain field equivalent to that which would be introduced by a single dislocation with Burgers vector equal to that of three elementary dislocations. (d) As the oppositely signed disclinations become further separated, the disorientation resulting from these defects increases.

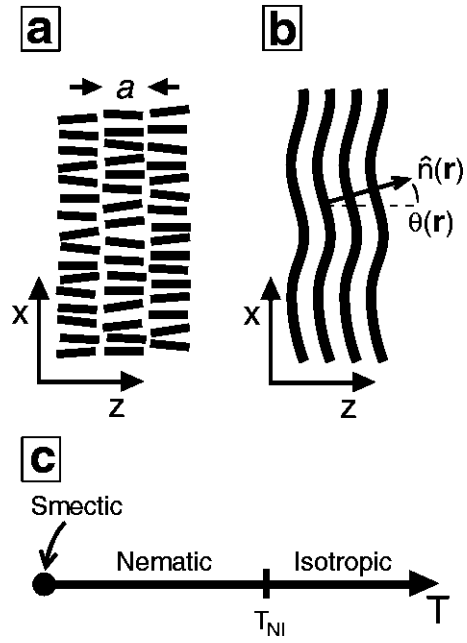

Figure 2. (a) Schematic representation of molecular (nematogen) arrangement within a two-dimensional smectic, which can be described as a mass density wave in the z direction. Only liquidlike correlations exist within each individual layer, i.e., in the x direction. (b) Schematic drawing of cylinders in the nematic phase, showing the local layer normal, $\hat{n}(\mathbf{r})$, and layer orientation, $\theta(\mathbf{r})$. Note that the position vector $\mathbf{r} \equiv (x,z)$. (c) A simple phase diagram applicable to 2D smectic systems. In layered materials, the apparent lower critical dimensionality is $d = 3$. Thus, in $d = 2$, phonons are sufficient to destroy layered (translational) order, pushing the smectic−nematic transition down to $T = 0$ K.[1] The nematic phase, which arises because of these fluctuations as well as the presence of dislocations, is characterized by long- or quasi-long-range order in the orientations of the layer normals. Upon heating through T_{NI}, this orientational order is lost due to a disclination unbinding process, producing an isotropic phase.

disorder transition temperature (ODT) and then quenching, rather than by slowly cooling. Our results show conclusively, however, that the monolayer order that can be achieved after long isothermal anneals is a steadily and strongly decreasing function of increasing temperature. The disorder results primarily from an equilibrium density of dislocations and, at higher temperatures, disclinations in the monolayer of cylinders, rather than from kinetic limitations. Remarkably, these results correspond closely to those predicted by Toner and Nelson more than 20 years ago.[1] The theory describes the melting of a two-dimensional smectic liquid crystal. While 2D smecticlike patterns have been shown to arise in a diverse set of systems, including, for example, ferrimagnetic domains in thin garnet films and Rayleigh−Benard convective rolls, our quasi-2D block copolymer monolayers provide an excellent model system for testing the theory. Figure 2a shows a 2D smectic in the $x-z$ plane in which a mass density wave persists in the z direction. Figure 2c presents a simple theoretical phase diagram for such a 2D smectic system. True smectic ordering is predicted to be possible only at $T = 0$, above which phonons are sufficient to destroy long-range translational order. This creates a "nematic" phase, where in the present case the local cylinder normal in the plane of the monolayer plays the role of nematic director, as shown in Figure 2b. Additionally, a finite density of thermally generated dislocations is predicted by Toner and Nelson to be present above $T = 0$. Since in 2D isolated dislocations are point defects, they are predicted to occur with density

$$n_D \approx a_c^{-2} \exp(-E_D/k_B T) \quad (1)$$

where a_c is the dislocation core radius and E_D is the energy required to create a dislocation.[1] In such a layered system the strain field of a dislocation decays exponentially with distance from the core, giving rise to a finite value of E_D even in an infinite 2D plane.[19]

Upon further heating, Toner and Nelson predict the 2D system to undergo a disclination unbinding process at some temperature T_{NI}, producing an isotropic phase in which both translational and orientational order are short range; i.e., the respective correlation functions decay exponentially with distance. During this nematic-to-isotropic phase transition, the tightly bound disclination pairs that make up individual dislocations become separated by a distance of one or more repeat spacings, creating disclinations as they are more commonly envisioned (Figure 1b,d). In this work, we show that the laterally confined cylinders studied here follow this phase diagram as the annealing temperature is increased, as determined from equilibrium densities of dislocations and disclinations as well as by quantitative measures of translational and orientational order. Equilibrium properties are investigated by comparing results of annealing initially well-ordered samples at a given

temperature with those obtained from samples cooled from the disordered state and annealed at the same temperature. While this paper was in preparation we learned that the group at Princeton have observed defect-controlled melting of initially well-ordered 2D arrays of block copolymer cylinders that are qualitatively similar to those that we report below.[20] Significantly, however, the nematic−isotropic transition that we observe occurs ~20 °C below the bulk (3D) order−disorder transition for our block copolymer as measured by small-angle X-ray scattering.

Experimental Section

Diblock Copolymer. Polystyrene-*b*-poly(2-vinylpyridine) (PS−PVP) with overall molecular weight $M_n = 26\,000$, polydispersity index 1.07, and mole fraction of PVP mers $f_{PVP} = 0.25$ was synthesized via anionic polymerization. 2-Vinylpyridine (Aldrich) was dried over calcium hydride and vacuum-distilled. Residual traces of water and alcohols were removed by the addition of a small amount of triethylaluminum (Aldrich) and distillation under a reduced pressure of purified nitrogen gas. The 2-vinylpyridine monomer was stored under dry nitrogen until use. THF was dried in a column packed with activated alumina and collected in a dried flask. A small amount of styrene monomer (Aldrich) was added to the flask, followed by excess *sec*-butyllithium (Aldrich). The orange color of the living styrene ion ensured that the solution was completely dry at that point, after which the THF was vacuum-distilled into a dried flask for the polymerization. The styrene monomer used in the polymerization was purified by addition of dibutylmagnesium (Aldrich) followed by vacuum distillation directly into the reaction flask containing the THF. After the styrene polymerization (initiated by *sec*-butyllithium), a small aliquot was removed for determination of the PS block molecular weight by gel permeation chromatography, and the 2-vinylpyridine monomer was introduced. The volume fraction of the PVP block was measured by elemental analysis, and the total molecular weight was calculated. In bulk, this copolymer orders into hexagonally packed cylindrical PVP core domains in a PS matrix, with a nearest-neighbor spacing of 22 nm.

Small-Angle X-ray Scattering. SAXS patterns were obtained at the Materials Research Laboratory X-ray facility at UCSB from a 0.8 mm thick compression-molded PS−PVP sample. The sample was molded within a copper washer, to one side of which had been attached a Kapton sheet using high-temperature compatible, solventless epoxy (Duralco 4701, Cotronics Corp.). The copolymer was then sealed in place using another Kapton sheet and the same epoxy. Care was taken to prevent epoxy from coming into contact with the copolymer sample or fouling the Kapton windows. This procedure ensured that no copolymer material was lost as the sample was heated. The sealed sample was put into an Instec heat stage, and the entire assembly was placed in the beam path for in-situ temperature-dependent measurements. The temperature was varied from 190 to 236 °C, and data from both heating and cooling were collected to check for reversibility. The sample temperature was held constant for 15 min at a given temperature to allow equilibration before turning on the X-ray beam, followed by 45 min of data collection. A fine focus (0.2 mm) Rigaku rotating anode generator provided copper Kα radiation (1.54 Å), the beam spot size of which was ~1 mm^2. A Bruker HI-STAR multiwire area detector, located 1.5 m from the sample, was used to record the scattering patterns.

Substrate Fabrication. Silicon oxide layers 20 nm thick were deposited onto native-oxide covered silicon wafers by plasma-enhanced chemical vapor deposition. A series of long (500 μm) channels were created in this layer by standard photolithography and etching in an inductively coupled CHF_3 plasma. The channels were etched down to the Si/SiO_2 interface, and the native oxide was allowed to regrow, resulting in a 20 nm channel depth. The plateaus separating the channels were universally ~1 μm, and although channels of varying width (1−10 μm) were created, we present here only results from 2 μm wide channels. Photoresist and etch residues were removed with thorough photoresist stripper treatment, followed by rigorous cleaning in 80 °C "piranha" etchant.

Film Deposition and Thermal Treatment. PS−PVP thin films were deposited via spin-coating from dilute (~1%) toluene solution. All thermal treatments were carried out in a high-vacuum furnace operating at base pressures $<10^{-6}$ mbar. Samples were quenched to below the glass transition temperature of both blocks of the copolymer ($T_g = 100$ °C) by quickly backfilling the vacuum chamber with high-purity nitrogen gas and placing the small (~0.25 cm^2) samples on an aluminum block at room temperature, a procedure that took ~10 s. Specifics of the various thermal treatments (ramp rates, soak temperatures, and soak times) are detailed later in the text.

The wetting conditions in this system are such that the PVP is strongly attracted to the silicon oxide interfaces, creating a uniform brush layer upon which subsequent layers of cylinders sit, while PS wets the vacuum interface. Thus, upon annealing above T_g, islands or holes[21−23] form in films where the initial thickness, h, does not satisfy the condition

$$h = n\alpha + \beta \tag{2}$$

where n is an integer, α is the thickness of one cylinder layer (approximately equal to the (10) plane spacing in bulk, 19 nm), and β is the brush thickness. We cast our films at a thickness less than $\alpha + \beta$ such that holes form in the cylinder monolayer in areas with no substrate topology. In the patterned regions, however, the holes in the channels act as sinks for excess material, and copolymer material from the mesas flows into the channels.[24] Films were spun-cast with thickness such that, after annealing, the channels contained a full monolayer and the mesas were covered only by the brush.

Copolymer Microstructure Imaging and Image Processing. The top surface of the film is smooth on a nanometer height scale. Thus, to reveal the cylinder ordering, the films were etched down to the PVP cylinder core midplane using the O_2^+ ion beam of a Physical Electronics 6650 dynamic secondary ion mass spectrometer (dSIMS). The primary beam, operated at 1 kV beam voltage and 20 nA beam current, was rastered over an 0.16 mm^2 area. A defocused, static 500 eV electron beam was concurrently directed at the beam crater in order to maintain charge neutrality. Etch depth was controlled by monitoring secondary ion counts of CN^-, which serves as a proxy for PVP volume fraction. The etch was stopped just past the first maximum in CN^- ion counts. The PVP cores etch slightly faster than their PS matrix, giving rise to a 1−2 nm height contrast that was subsequently imaged using a Digital Instruments MultiMode scanning force microscope operated in tapping mode. Unfortunately, the destructive nature of this sample imaging technique prevents further annealing of a given sample.

The stretching or compression of SFM images in the slow scan direction has been documented.[25] In the case of the randomly oriented 2D cylinder arrays we observed at higher temperatures, this effect was observed in the Fourier transforms of the images; what should be an isotropic, circular Fourier transform was found to be elliptical. All such images were digitally stretched or compressed to recover this isotropy. In the case of images showing aligned cylinders, no such correction was possible (or necessary, for that matter, since the cylinder axes were deliberately aligned with the slow scan axis).

Defect Counting. Although automated defect detection is possible,[17] and was implemented, it was found that the reliability of the results of this process greatly depended on the quality of the image used as input. Specifically, image noise, even after Fourier filtering, often introduced an unacceptable number of "false positives". Manual defect counting, though laborious, proved to be more reliable for the images we were able to obtain. To facilitate this process, images (1 μm^2, from the center portion of the channel) were imported into Adobe Illustrator, the cylinder cores were carefully traced, and the original image was removed. The defects in these

tracings were easily classified as either dislocation, $+1/2$ disclination, or $-1/2$ disclination and counted. Since we determined that the densities of $+1/2$ and $-1/2$ disclinations in any sample were approximately equal as expected, we report hereafter only the $+1/2$ disclination density.

Orientational Correlation Function Calculation. Orientational correlation functions were calculated using 1 μm wide $\times$ 2 μm tall SFM images, taken from the center portion of the channel. Because of some combination of nonuniformity in the etching process and instrumental difficulties imaging these samples with SFM, even the best images contain some long wavelength background and significant amounts of short wavelength noise. Before automated determination of the cylinder normals, the images were therefore subjected to careful Fourier filtering,[25] followed by gray scale thresholding and low-pass filtering. The orientation field $\theta(\mathbf{r})$ of these normals was then determined by measuring the local gray scale intensity gradient, following the work of Harrison et al.[17] (The orientation angles were defined with respect to the image horizontal axis, although any arbitrarily chosen direction would yield identical results.) The orientational order parameter field $\psi_2(\mathbf{r})$ was subsequently calculated according to

$$\psi_2(\mathbf{r}) = \exp[2i\theta(\mathbf{r})] \tag{3}$$

The factor of 2 is included in the exponential to reflect the 2-fold symmetry of the system.

From this order parameter field, the orientational correlation function

$$g_2(\mathbf{r}) = \langle \psi_2{}^*(\mathbf{0})\, \psi_2(\mathbf{r}) \rangle \tag{4}$$

was calculated, where the angular brackets imply an averaging over all pairs of points. (Note the subtle change in notation, as "$\mathbf{r}$" refers here to the vector separating each pair of points being correlated, rather than the position vector (x,z) in the order parameter field.) While averages of $g_2(\mathbf{r})$ for specific directions of $\mathbf{r}$ are possible to obtain, we simply present below the azimuthal average of this function, $g_2(r)$.

Translational Correlation Function Calculation. The most suitable input for the calculation of translational correlation functions turned out to be the cylinder tracings produced for counting defects, as just described. The translational order parameter is

$$\psi_{\mathbf{G}}(\mathbf{r}) = \exp[i\mathbf{G}\cdot\mathbf{r}] \tag{5}$$

where $\mathbf{G}$ is the dominant wave vector determined from the Fourier transform of a given image. The order parameter was then correlated in the usual way:

$$g_{\mathrm{G}}(\mathbf{r}) = \langle \psi_{\mathrm{G}}{}^*(\mathbf{0})\, \psi_{\mathrm{G}}(\mathbf{r}) \rangle \tag{6}$$

where again we have changed notation such that $\mathbf{r}$ refers here to the vector separating the points being correlated, and the results azimuthally averaged to give $g_{\mathrm{G}}(r)$.

Computer Simulation Methods. We employ self-consistent-field theory (SCFT), a type of mean-field theory,[26−29] to model the temperature-dependent compressional modulus $B(T)$ of the cylinder-forming diblock copolymer monolayers considered in this work. This theory, which has been able to successfully encapsulate important features of the equilibrium behavior of block copolymer melts, reduces the problem of calculating the partition function for an entire system of interacting chains to that of finding a constrained partition function $q(r,s)$ for a single chain segment beginning at point r of polymerization index sN in a spatially fluctuating inhomogeneous chemical potential field. In a diblock copolymer with a volume fraction f of A blocks, $q(r,s)$ satisfies the modified diffusion equation

$$\frac{\partial q(\mathbf{r},s)}{\partial s} = R_{\mathrm{g}}{}^2\nabla^2 q(\mathbf{r},s) - w_i(\mathbf{r})\, q(\mathbf{r},s) \tag{7}$$

subject to the initial condition $q(\mathbf{r},0) = 1$, where i = A for $s < f$, i = B for $s > f$, and R_{g} is the unperturbed radius of gyration. The local reduced density operators $\rho_{\mathrm{A}}(\mathbf{r})$ and $\rho_{\mathrm{B}}(\mathbf{r})$ may be calculated via

$$\rho_{\mathrm{A}}(\mathbf{r}) = \frac{1}{Q}\int_0^f \mathrm{d}s\; q(\mathbf{r},s)\, q^\dagger(\mathbf{r},s)$$

$$\rho_{\mathrm{B}}(\mathbf{r}) = \frac{1}{Q}\int_f^1 \mathrm{d}s\; q(\mathbf{r},s)\, q^\dagger(\mathbf{r},s) \tag{8}$$

where $q^\dagger(\mathbf{r},s)$ is the solution to (7) subject to $q^\dagger(\mathbf{r},1) = 1$. Q is the single-chain partition function whose relationship to $q(\mathbf{r},s)$ is given by

$$Q = \frac{1}{V}\int \mathrm{d}\mathbf{r}\; q(\mathbf{r},1) \tag{9}$$

At a saddle point these fields must satisfy

$$w_{\mathrm{A}} = \chi N\rho_{\mathrm{A}}(\mathbf{r}) + \xi(\mathbf{r}) \tag{10}$$

$$w_{\mathrm{B}} = \chi N\rho_{\mathrm{B}}(\mathbf{r}) + \xi(\mathbf{r}) \tag{11}$$

$$\rho_{\mathrm{A}}(\mathbf{r}) + \rho_{\mathrm{B}}(\mathbf{r}) = 1 \tag{12}$$

$$\rho_{\mathrm{A}}(\mathbf{r}) = -\frac{V}{Q}\frac{\partial Q}{\partial w_{\mathrm{A}}} \tag{13}$$

$$\rho_{\mathrm{B}}(\mathbf{r}) = -\frac{V}{Q}\frac{\partial Q}{\partial w_{\mathrm{B}}} \tag{14}$$

where $\xi(\mathbf{r})$ is a pressure field chosen to satisfy (12). At a saddle point the single chain free energy F may be calculated as

$$\frac{F}{k_{\mathrm{B}}T} = \frac{1}{V}\int \mathrm{d}\mathbf{r}\; (\chi N\rho_{\mathrm{A}}(\mathbf{r})\, \rho_{\mathrm{B}}(\mathbf{r}) - w_{\mathrm{A}}\rho_{\mathrm{A}}(\mathbf{r}) - w_{\mathrm{B}}\rho_{\mathrm{B}}(\mathbf{r})) - \ln Q \tag{15}$$

The modified diffusion equation was solved using the combined real-space/Fourier-space, or "pseudospectral", algorithm as described in detail elsewhere[30]

$$q(\mathbf{r}, s + \Delta s) \cong \mathrm{e}^{-w_i(\mathbf{r})\Delta s/2}\mathscr{F}^{-1}(\mathrm{e}^{-\Delta s R_{\mathrm{g}}{}^2\mathbf{k}^2}\mathscr{F}(\mathrm{e}^{-w_i(\mathbf{r})\Delta s/2}q(\mathbf{r},s))) \tag{16}$$

where $\mathscr{F}$ denotes the Fourier transform. Saddle-point (mean-field) configurations were calculated using an iterative semi-implicit relaxation scheme devised by Ceniceros and Fredrickson.[31]

Here the PS−PVP monolayer is represented as a conformationally symmetric $f = 0.25$ AB linear diblock copolymer. The linear array of cylinders in the plane of the substrate is essentially equivalent to a 2D periodic array of cylinders situated on a square lattice with $p4m$ plane group symmetry; we neglect the effects the polymer/substrate and polymer/air interfaces that are encountered in the experimental case, which to a good approximation serve only to shift the free energy by a constant. The free energy of a single unit cell of such an arrangement was calculated to within $10^{-8}k_{\mathrm{B}}T$ using (7)−(16) with a 96 $\times$ 96 grid and a value of $\Delta s = 0.006$ in (10), where the initial chemical potential fields w_{A} and w_{B} were constructed using the first harmonic of the $p4m$ plane group. Iterative adjustment of w_{A}, w_{B}, and the length scale of the simulation volume allows the simultaneous satisfaction of (4)−(8) and the requirement of vanishing internal stress, which may be calculated pseudospectrally according to

$$\sigma_{ij} = \left(\frac{2k_{\mathrm{B}}TR_{\mathrm{g}}{}^2}{VQ}\right)\int \mathrm{d}\mathbf{r}\int_0^1 \mathrm{d}s\; q(\mathbf{r},s)\nabla_i\nabla_j q^\dagger(\mathbf{r},s) \tag{17}$$

Calculations conducted in this manner yield a minimal free

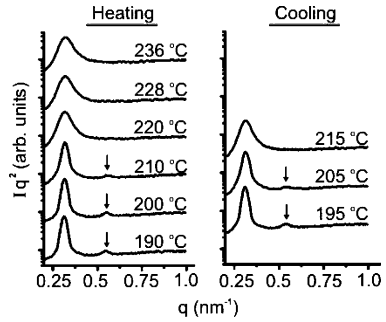

Figure 3. Results from azimuthally averaged SAXS patterns obtained from the PS−PVP sample as a function of temperature. Data from the heating cycle are on the left and from the cooling cycle are shown at right. At 210 °C and below, the $\sqrt{3}q^*$ peak (indicated by arrows) indicates relatively good hexagonal ordering in the cylinders. Above 210 °C, the $\sqrt{3}q^*$ peak disappears and the q^* peak broadens significantly.

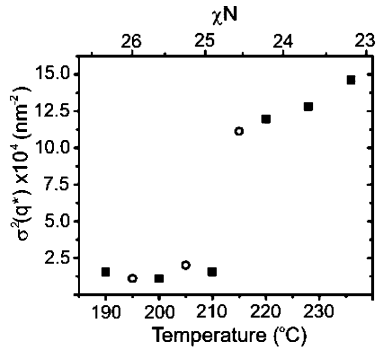

Figure 4. Summary of SAXS data showing the temperature dependence of the square of the q^* peak width. The discontinuous jump in $\sigma(q^*)^2$ between 210 and 215 °C indicates the ODT. Additionally, the coincidence of heating (filled squares) and cooling (open circles) data onto the same lines indicates that the ordering/disordering process occurred reversibly.

energy F^* with respect to the constraint of $p4m$ symmetry at some preferred cell size $d_x = d_y = d^*$.

The compressional modulus $B(T)$ is related to the change in free energy δF arising from a uniaxial extension ϵ from the initial $p4m$ state. For small extensions, a linear stress−strain relationship may be anticipated so that the appropriate expression for δF becomes

$$\frac{\delta F}{RT} = \frac{1}{2}\left(B(T)\frac{\bar{V}}{RT}\right)\epsilon^2 \tag{18}$$

and $B(T)$ may be evaluated via

$$B(T) = \frac{RT}{\bar{V}}\frac{\partial^2(\delta F)}{\partial \epsilon^2} \tag{19}$$

where $\bar{V}$ is the molar volume. The function $\delta F(\epsilon)$ may be evaluated within the SCFT by varying the shape of the simulation cell, i.e., changing d_x at fixed $d_y = d^*$. Tyler and Morse have made similar calculations regarding the linear elasticity of bulk cubic block copolymer phases in a recent publication.[32]

Results and Discussion

Temperature Dependence of Ordering in Bulk. Before presenting results from the 2D studies, we present results from 3D samples of the same copolymer to establish a useful basis for comparison. Figure 3 displays azimuthally averaged SAXS scattering patterns of our PS−PVP block copolymer, obtained during both heating and cooling. Scattering data from successive temperature steps are offset by one decade from each other for easy visualization. Qualitatively, at temperatures below 215 °C, relatively sharp q^* and $\sqrt{3}q^*$ peaks are visible, indicating a reasonably well-ordered hexagonally packed cylinder structure. At 215 °C and above, the $\sqrt{3}q^*$ peak disappears and the q^* peak broadens significantly, signaling the disappearance of the hexagonal structure. In Figure 4, the square of the q^* peak half-width is plotted against T. Values of the product $\chi(T)N$, where N is the degree of polymerization of the diblock copolymer and $\chi(T) = -0.033 + 63/T$ is the Flory−Huggins segment−segment interaction parameter for PS−PVP,[33] are plotted on the top axis. Data points from both heating and cooling fall on the same lines, indicating that the sample was sufficiently equilibrated at each temperature step and that the entire process is reversible. A large discontinuous jump in $\sigma^2(q^*)$ occurs between 210 and 215 °C, providing a clear indication of the order−disorder transition (ODT) at ∼212.5 ± 2.5 °C.

Laterally Confined Monolayer Film Results. a. Films Annealed above the Bulk ODT. In the laterally confined monolayer films, samples annealed above the bulk ODT show highly disorganized cylinder order, regardless of the presence of the confining channel walls, as shown in Figure 5a, an SFM micrograph of a sample annealed for 1 h at 215 °C. One edge of the channel is visible on the left side of the image. The film exhibits a dislocation density of ∼70 μm^{-2} and a comparable disclination density. Figure 6 (star symbols) shows the azimuthally averaged orientational correlation function from the sample. The x-axis has been normalized by the cylinder repeat spacing, $a = 22$ nm. Fitting to $g_2(r) = \exp(-r/\xi_2)$ yields the orientational correlation length $\xi_2 = 37$ nm or $\xi_2/a = 1.7$. At this temperature and above, this pattern does not coarsen, and the densities of dislocation and disclinations do not decrease, after longer annealing time.

b. Films Slowly Cooled from above the Bulk ODT and Then Quenched. A set of samples was prepared by heating them above 215 °C, subsequently cooling slowly (∼1 °C/min), and quenching each sample at a given temperature on this cooling trajectory. In these samples, increasingly better order was found as the slow cooling was allowed to proceed further, as can be seen for example in Figure 5b, from a sample quenched at 150 °C. Note that there are no disclinations in the image, and the sample exhibits a high degree of orientational order. The dislocation density in this sample is ∼8 μm^{-2}. Figure 6 displays $g_2(r)$ for this sample (squares) as well as one quenched at 185 °C, in which $n_{\text{dislocations}} \approx 22$ μm^{-2} and $n_{\text{disclinations}} \approx 4$ μm^{-2} (circles). Qualitatively different behavior in the orientational correlation functions for these latter two samples relative to that of the sample quenched from 215 °C is observed. The orientational correlation function $g_2(r)$ can no longer be fit to a simple exponential decay.

c. Films Subjected to Thermal Treatments Designed To Yield Equilibrium Structures. To probe the equilibrium behavior of the system, two sets of complementary samples were produced. The first set, referred to here as the "cooling experiments", was heated above the bulk ODT, slowly cooled (∼1 °C/min) to a given temperature, annealed at that temperature for 4 h, and quenched. The second set of samples ("heating experiments") were preordered by heating above the bulk ODT and slowly cooling to 100 °C (the

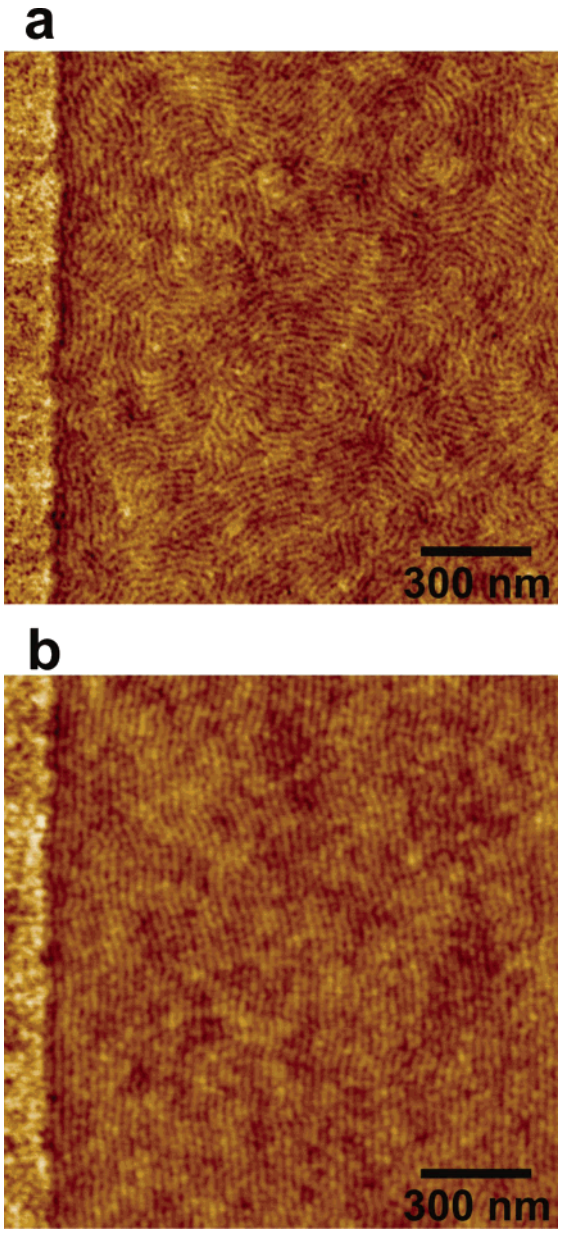

Figure 5. (a) SFM image (2.25 μm^2) of a sample annealed at 215 °C for 1 h showing highly disorganized cylinders. One edge of the confining well is visible on the left. (b) Similar image; however, after the 1 h anneal at 215 °C, the sample was cooled (1 °C /min) to 150 °C and quenched. After this cooling step, the cylinders have adopted the orientation of the wall (visible at left).

glass transition temperature of the PS−PVP block copolymer) over the course of 12 h. They were each then heated to a given temperature, annealed for 4 h, and quenched. Figure 7 summarizes these annealing protocols. As will be shown, results from the cooling and heating experiments were consistent, implying that the degree of ordering, defect density, etc., obtained at each temperature approach the equilibrium properties of the system at that temperature.

Figure 8 displays several representative 1 μm^2 square images taken in the center of the channel of films from the heating experiments, beginning with a sample imaged after the preannealing treatment (Figure 8a). For practical purposes of plotting the properties of this sample, we label it as "100 °C", the PS−PVP T_g. This sample shows superb orientational ordering and no

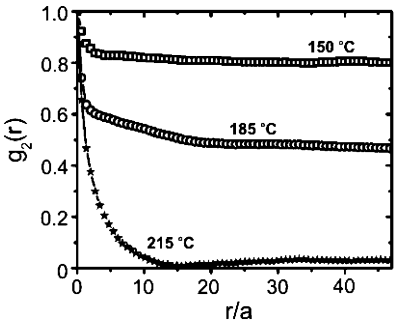

Figure 6. Azimuthally averaged orientational correlation function results for laterally confined cylinder monolayers annealed above 215 °C, cooled (~1 °C/min) to the indicated temperatures, and immediately quenched.

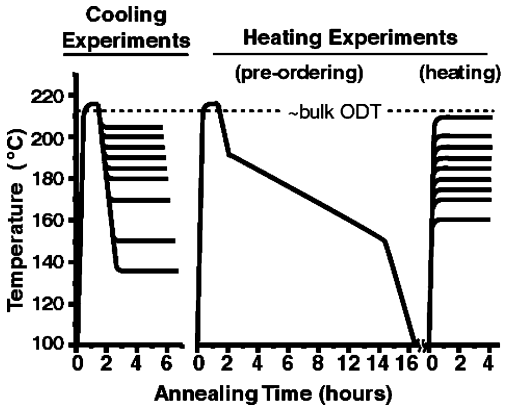

Figure 7. Details of thermal annealing protocols for cooling (left) and heating (right) sample sets. Note that after the long "preordering" annealing phase in the heating sample set these samples were heated from the well-ordered state.

defects within the field of view. All other samples in the heating experiment presumably began in this highly ordered state. After reannealing at 180 °C (Figure 8b), a high degree of orientational order is maintained, although a significant number of dislocations are present. Upon further increases in temperature, a finite density (~30 μm^{-2}) of unbound disclinations begin to cause the first significant disorientations (190 °C, Figure 8c), until finally the cylinder array becomes highly disoriented and disclination-rich (200 °C, Figure 8d). Images from the cooling experiments (not shown) display the same temperature-dependent behavior.

d. Dislocation and Disclination Density Measurements. The results of our defect counting analysis of the image of films from the heating and cooling experiments confirm the assertion that a near-equilibrium population of defects is produced by both types of experiment. As shown in Figure 9a, the dislocation density rises slowly between 100 and 180 °C and then increases much more rapidly at higher temperatures. While the dislocation density after heating and cooling is similar at all temperatures, it is somewhat larger for the samples produced by cooling compared to that produced by heating at temperatures below 180 °C. This result indicates that while an equilibrium dislocation density is approached, it is never quite achieved in this temperature range. The disclination density, on the other hand, remains at or very near zero until 180 °C, above which it increases dramatically as shown in Figure 9b. These plots of defect density vs temperature are remarkably consistent with the predictions of Toner and Nelson.[1] Below a certain temperature, 180 °C in

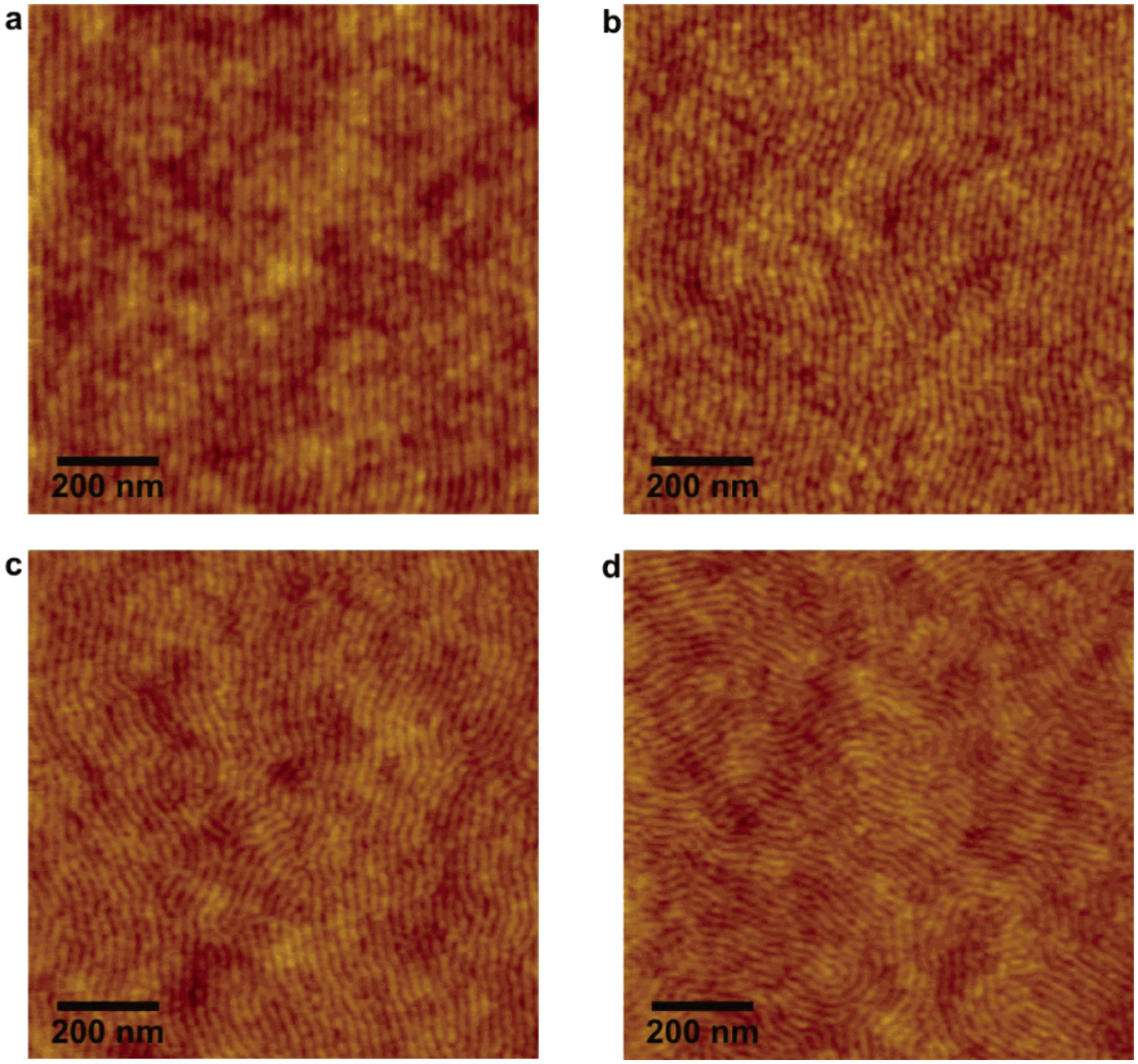

Figure 8. SFM images (1 μm^2) of etched, laterally confined PS−PVP cylinder monolayer samples from the heating experiments. (a) Preordered sample ("100 °C") showing excellent orientational order and no topological defects within the field of view. Preordered samples subsequently annealed at 180 °C (b) and 190 °C (c) show progressively more defects and less orientational order, until at 200 °C a highly disoriented, highly defective monolayer is observed (d). The images were taken from the middle portion of the 2 μm wide channels.

our case, the monolayer of cylinder domains has an increasing dislocation density but no disclinations. In the Toner−Nelson nomenclature this regime consists of the nematic phase. Above a certain temperature, the nematic-to-isotropic transition temperature T_{NI}, some of these dislocations can thermally dissociate into their component disclinations, and the system is predicted to undergo a transition to the isotropic phase. This progression of defect formation is exactly what we observe. The thermal generation of dislocations should give rise to a dislocation density that increases as $\exp(-E_D/k_BT)$ (1), where E_D is the energy of the dislocation. Figure 10 shows that between 135 and 180 °C roughly such an exponential increase in dislocation density occurs.

Chandrasekhar and Ranganath[34] derived a simple expression for the energy per unit length ϵ_D of a dislocation in a smectic liquid crystal, which, because the strain field is short-ranged,[35] does not depend on an outer cutoff radius as does the energy of a dislocation in an atomic crystal, viz.

$$\epsilon_D = \frac{\lambda b^2}{2a_c}B + \epsilon_c \qquad (20)$$

whose first term describes the contribution of the elastic strain field around the dislocation and whose second term is the energy that results from the local perturbation of polymer chains at the dislocation core. The elastic constant B is the compressional modulus normal to the layers, b is the dislocation Burgers vector, and a_c is the radius of the dislocation core. The "penetration depth" λ is defined in terms of the ratio of the Frank constant for bending the cylinders (splay of the polymer molecules) K_1 to the compressional modulus B, as $\lambda = (K_1/B)^{1/2}$. Amundson and Helfand[36] have estimated that $\lambda \approx 0.1a$ for a lamellar block copolymer whose lamellar spacing is a and roughly independent of temperature as the ODT is approached. If we set $b \approx a_c \approx a$ for our 2D cylinder layer we can simplify eq 20 to read

$$E_D \approx \alpha\left(\frac{\lambda a}{2}B(T) + \epsilon_c\right) \approx 0.05\alpha a^2 B(T) + \alpha\epsilon_c \qquad (21)$$

where α is the layer thickness and the right-most equality results from substituting the Amundson−Helfand result for λ. From the simulations described above we have extracted values for $B(T)$ as the ODT is

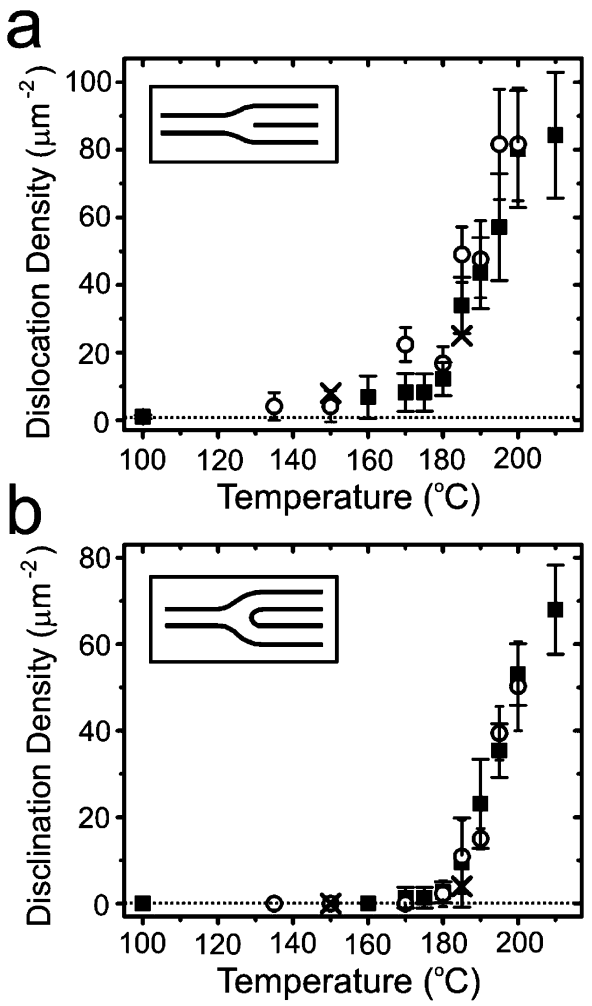

Figure 9. Dislocation (a) and $+^1/_2$ disclination (b) densities plotted against annealing temperature for heating (filled squares) and cooling (open circles) experiments. Also shown are defect densities for the samples quenched immediately after cooling, as described in the text relevant to Figures 5 and 6 (×'s). In the defect schematics drawn here, cylinder cores are represented by black lines.

approached and find that

$$B(T) \approx B_0 - B'T \tag{22}$$

where $B_0 = 537$ kPa and $B' = 0.58$ kPa/K. The slope of the straight line in Figure 10 over the range 135−180 °C should be thus $-(0.05\alpha a^2 B_0 + \alpha\epsilon_c)/k_B$ where $\alpha = 19$ nm and $a = 22$ nm. The term $-0.05\alpha a^2 B_0/k_B = -17900$ K, a number that is in order of magnitude agreement with the experimental value for the slope, -6000 ± 2000 K, of the line in Figure 10. This comparison also assumes that the core energy of the dislocation is small enough that it can be disregarded. Clearly, more elaborate simulations will be needed to determine B, λ, and ϵ_c more accurately, an endeavor that is certainly possible given current SCFT methodology for studying defect states. For instance, Netz et al.[37] and Matsen[38] have made calculations of chevron defects in lamellar block copolymers, reproducing the "chevron" to "omega" transition as the angle between grains is increased. However, we are encouraged by the fact that the simple calculation reported here yields an approximate dislocation energy that predicts a strong temperature dependence of the dislocation density that is close to the experimental result.

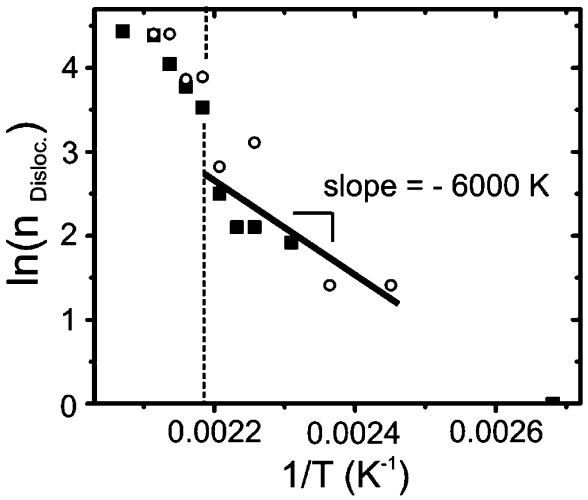

Figure 10. Semilogarithmic plot of the dislocation density data presented in Figure 9a vs inverse temperature. Data from temperatures at which we observe a significant disclination density (to the left of the dotted vertical line) was disregarded for the linear fit (solid line), as was the data point at 100 °C. This line yields $E_D/k_B = 6000 \pm 2000$ K; at the annealing temperatures here, E_D corresponds to approximately $13-15k_BT$.

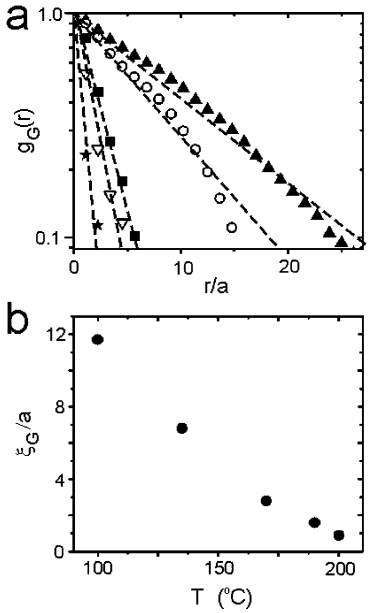

Figure 11. Selected translational correlation function results for confined cylinder monolayer samples equilibrated at the following temperatures: "100 °C" (filled triangles, heating), 135 °C (open circles, cooling), 170 °C (filled squares, cooling), 190 °C (open diamonds, cooling), and 200 °C (filled stars, cooling). Exponential decay in $g_G(r)$ is observed in all cases (dashed line fits), with progressively shorter correlation lengths, ξ_G, determined from a fit to $g_G(r) = \exp(-r/\xi_G)$, upon increasing temperature (b).

e. Translational and Orientational Correlation Function Analysis. Translational correlation function data for samples at several temperatures are shown in Figure 11a plotted on a semilogarithmic scale. At all temperatures it can be seen that the translational correlation function decreases exponentially with r/a; i.e., $g_G(r)$ shows only short-range order

$$g_G(r) = \exp(-r/\xi_G) \tag{23}$$

where ξ_G is the translational correlation length. How-

ever well ordered the sample depicted in Figure 8a appears, thermal fluctuations (phonons) are still sufficient to produce a cylinder array with only short-range order with a correlation length of $\xi_G \approx 12a$. As the temperature is increased, this translational correlation length decreases as shown in Figure 11b, eventually falling to $\sim 1a$ at 200 °C. This behavior is qualitatively what would be expected for a 2D smectic ("nematic") as the temperature is increased.

On the other hand, as seen directly from the images in Figure 8a,b, samples equilibrated at lower temperatures exhibit a high degree of orientational ordering. Representative orientational correlation function results for both the heating and cooling experiments are presented in Figure 12, as a log−log plot in Figure 12a and a semilog plot in Figure 12b. Universally, samples equilibrated at lower temperatures exhibit a $g_2(r)$ that decreases roughly as a straight line on a log−log plot, implying that $g_2(r)$ shows a power law decay with r as r increases, i.e.

$$g_2(r) \approx (r/a)^{-\eta_2(T)} \tag{24}$$

Materials with correlation functions that decay as a power law are said to exhibit quasi-long-range order, order that can be characterized by a temperature-dependent power law exponent $\eta_2(T)$. Below a temperature of 195 °C such a power law relation holds with exponents that increase with increasing temperature, as shown in Figure 12c. At temperatures above 195 °C the fit of $g_2(r)$ to an exponential decay, i.e., $g_2(r) = \exp(-r/\xi_2)$, is much better as can been seen in Figure 12b. Thus, at these temperatures the orientational order is short range, and while the correlation lengths decrease with increasing T, the array of cylinders is essentially isotropic. The combination of quasi-long-range orientational order and short-range translational order in samples equilibrated at $T \leq 190$ °C is the hallmark of the 2D "nematic" phase so we conclude that a transition from the "nematic" to the isotropic phase of the 2D cylinder array occurs at a temperature close to 195 °C. The question arises whether the isotropic 2D phase we observe above 195 °C is the analogue of the 3D isotropic or disordered phase. We observe no further qualitative changes in order, and little further decrease in translational or orientational correlation length, up to temperatures approaching 250 °C, well above the 3D ODT. We believe, but cannot yet prove, that the local cylinder order we observe in this range, e.g., Figure 5a, is the result of fluctuations frozen when we quench the cylinder array below its glass transition temperature. If this hypothesis is correct, the "nematic"-to-isotropic transition temperature of the 2D layer of block copolymer cylinders corresponds to its order−disorder transition temperature, a temperature that lies well below the 3D order−disorder temperature of ~212 °C. That reducing the dimensionality of the system down to (quasi) 2D lowers the nematic-to-isotropic transition temperature, T_{NI}, is demonstrated succinctly in Figure 13. This sample, which was equilibrated at 205 °C (between the bulk ODT and the value of 195 °C that we take for T_{NI}), was made with a slightly thicker PS−PVP film such that regions with one layer of cylinders in the channel coexist with regions ("islands") with two layers of cylinders in the channel. In the areas with monolayer cylinder coverage, the cylinder array is isotropic, as we have just described. In the areas with bilayer cylinder coverage, however, the cylinders are highly ordered.

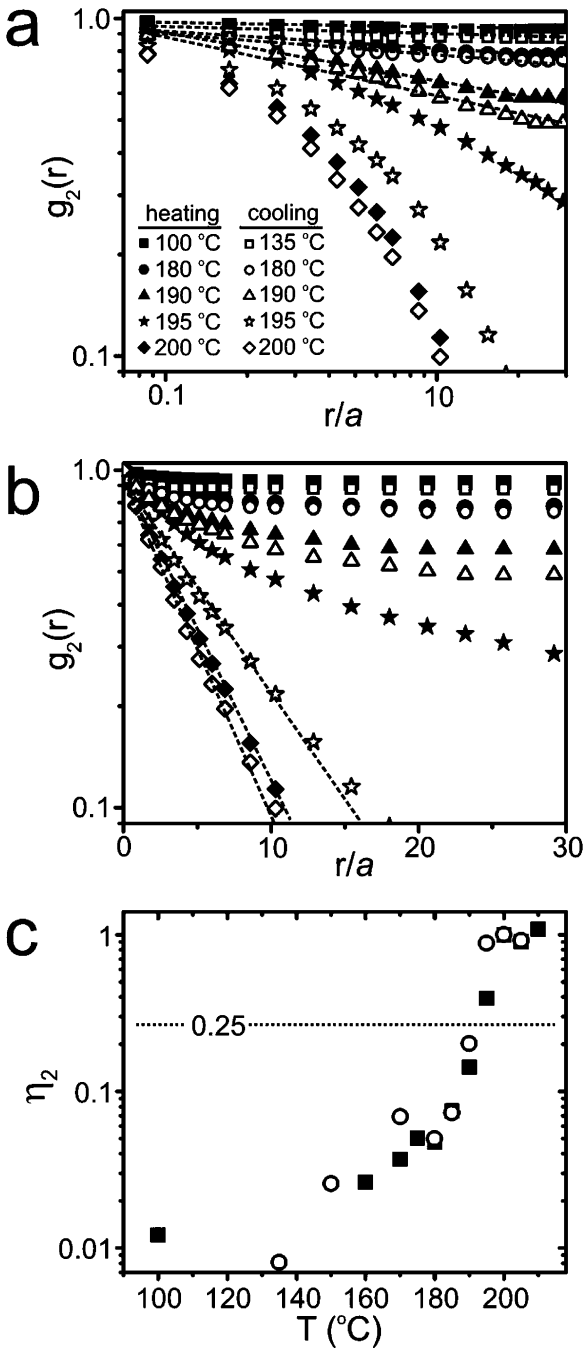

Figure 12. (a, b) Azimuthally averaged orientational correlation function results for the cooling experiment (open symbols) and the heating experiment (filled symbols). Data from the following temperatures are shown: 200 °C (diamonds), 195 °C (stars), 190 °C (triangles), 180 °C (circles), 135 °C (cooling, open squares), and "100 °C" (heating, filled squares). Results are plotted on a log−log scale in (a), showing algebraic decay in $g_2(r)$ for temperatures of 190 °C and lower, i.e., $g_2(r) \sim r^{\eta_2(T)}$ (dashed line fits). Results are plotted on a semilog scale in (b), demonstrating the exponential decay of $g_2(r)$ at 200 and 195 °C (cooling) (dashed line fits). (c) Algebraic decay exponent $\eta_2(T)$, obtained from fitting $g_2(r)$ data shown in (a). The dotted line at $\eta_2 = 1/4$ represents a condition set forth by Toner and Nelson for the nematic−isotropic transition. η_2 steadily increases over the temperature range of the experiments, exceeding $1/4$ at ~192 °C.

Toner and Nelson predict that the nematic-to-isotropic transition occurs when the temperature is high enough that the disclination pairs of individual dislocations unbind. We observe that the density of disclinations increases abruptly from near 0 at about 180 °C in both

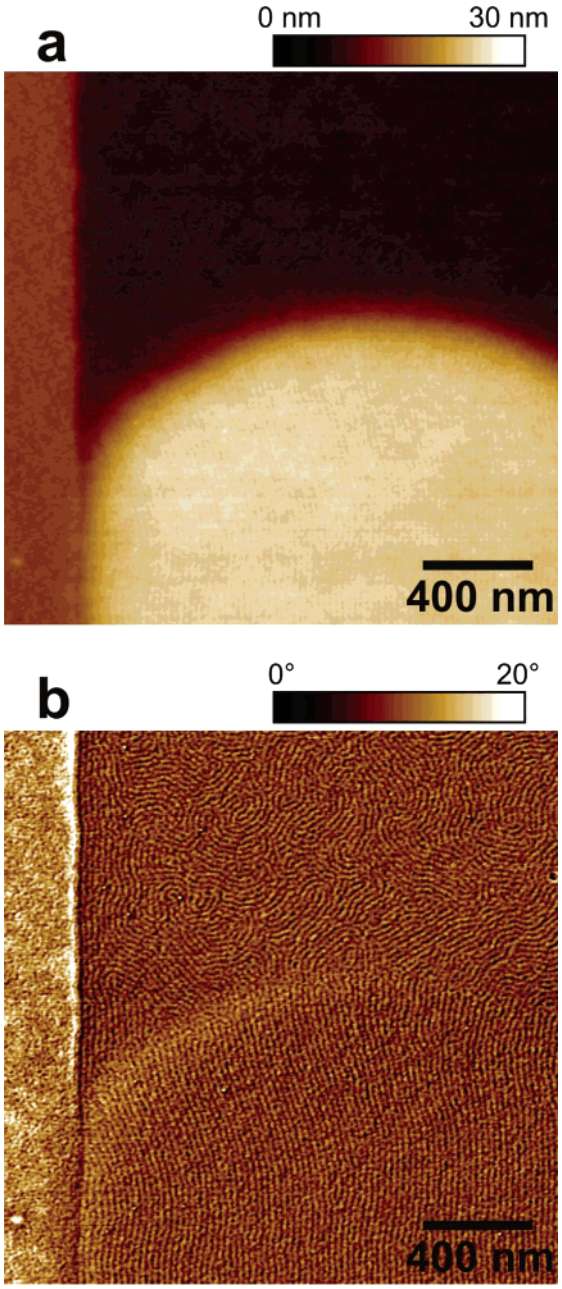

Figure 13. Height (a) and phase (b) scanning force microscopy images showing the effect of reduced dimensionality on the ordering of laterally confined cylinders. This sample is a slightly thicker film showing a region with monolayer coverage (top portion of images) adjacent to a region with a bilayer of cylinders (bottom portion) and was annealed above the bulk ODT, cooled slowly (~1 °C/min) to 205 °C, and held at 205 °C for 4 h. One edge of the channel is visible on the left side of the images. In the area of bilayer coverage, the cylinders in the second layer show a high degree of ordering, while the cylinders in the area of monolayer coverage are isotropic.

heating and cooling, significantly below the 195 °C we take to be T_{NI}. On the other hand, Toner and Nelson predict that the transition occurs at the temperature where the power law exponent $\eta_2(T)$ exceeds 0.25 (shown as the dotted line in Figure 13c). This occurs at about 192 °C, in good agreement with our value for T_{NI}. We observe that the great majority of the disclinations seen in our monolayers between 180 and 195 °C occur as close pairs, an example of which is shown in Figure 1b where the $+1/2$ and $-1/2$ disclination are separated by 1.5 cylinder spacings ($1.5a$). As can be seen qualitatively in Figure 1b, the long-range disturbance produced by such a disclination close pair is not dramatically more than that produced by a dislocation (Figure 1a). In fact, as can be seen by comparing Figure 1b with Figure 1c, the long-range displacement field of the disclination close pair is equivalent to that of a dislocation with a Burgers vector 3 times as long as that of the single dislocation in Figure 1a.[39] Increasing the distance between disclinations in the pair expands substantially the range of disturbance in the orientational order (Figure 1d). The data suggest that while disclination close pairs begin to be thermally generated at 180 °C, they do not dissociate significantly until 195 °C, where we see the first appearance of short-range orientational order. To be concrete, at 190 °C and below, the vast majority of the observed disclination pairs have component disclinations that are separated by a distance of $1a$ or less, and the greatest separation between opposite poles of the disclination pair that we have observed is $2a$. On the other hand, at 195 °C and above, we regularly observe disclination pairs in which the component disclinations are separated by $2.5a$ or more. This situation is analogous to what is observed at the transition from the hexagonal 2D crystal to the hexatic where dislocation close pairs are observed but which then dissociate at higher temperatures to form the hexatic phase.[25]

Our experiments occur within a channel of width 2 μm. Given the very short translation correlation lengths ($<12a$) observed, it is unlikely that the edges of the channel have any effect on the translational order. However, obviously at the lowest temperatures these edges profoundly affect the orientational order, even in the 1 μm $\times$ 1 μm central region of the channel where the SFM images were obtained. Dislocations, which are responsible for most of the disorder at relatively low temperatures, are repelled at short range from the hard edges by an image force (from a dislocation of the same Burgers vector).[35] Disclinations, which have longer range strain fields, are repelled from the edges by similar, but longer range, image forces.[39] Thus, one might imagine that the presence of such edges would stabilize the "nematic", much as the presence of similar walls stabilizes the hexatic in arrays of block copolymer spheres,[40] resulting in the "nematic"-to-isotropic transition temperature that we measure being somewhat above the T_{NI} that would be observed in a 2D cylinder array of infinite extent. While the details of the edge effects in our system are a subject for future characterization, the basic observations we report here should be unaffected, namely the gradual injection of disorder into the cylinder array by thermal generation of dislocations as the temperature is increased, followed by an unbinding of the disclinations in some of these dislocations to form an isotropic cylinder array at a temperature significantly below the 3D order−disorder transition in the bulk block copolymer.

Conclusion

The graphoepitaxially ordered diblock copolymer cylinder monolayers studied here, though possessing the local symmetry of a 2D smectic, do not display the long- or quasi-long-range translational order necessary to be correctly called such. Instead, in agreement with theory, fluctuations and a finite density of thermally generated dislocations disrupt translational order, yet persistent order in the cylinder orientations remains, yielding a

phase more properly described as a nematic. As the temperature is raised, an increasing density of dislocations is observed, until finally disclinations begin to appear, signaling the onset of the transition to an isotropic phase, characterized by a high density of disclinations and orientational correlations that decay exponentially, with an orientational correlation length of only a few repeat spacings. This N−I transition occurs ∼20 °C lower than the corresponding order−disorder transition observed in the bulk. These results carry implications for the application of block copolymer cylinders for nanolithography. Specifically, if true translational order is necessary, additional tools to achieve that order will need to be developed and employed. Presumably those tools will require patterning the substrate on length scales of similar order of magnitude as the copolymer repeat spacing.

Acknowledgment. This work was supported by the National Science Foundation DMR-Polymers Program under Grant DMR03-07233 and made use of MRL Central Facilities supported by the NSF MRSEC Program under Award No. DMR00-80034. We gratefully acknowledge several useful discussions with Professor David Nelson. M.R.H. is grateful to Professor Matthew Turk, Gila Stein, and Alexander Hexemer for technical assistance regarding image analysis and to Ryan Hayward for assistance in performing the SAXS measurements.

References and Notes

(1) Toner, J.; Nelson, D. R. *Phys. Rev. B* **1981**, *23*, 316−334.
(2) Park, M.; Harrison, C.; Chaikin, P. M.; Register, R. A.; Adamson, D. H. *Science* **1997**, *276*, 1401−1404.
(3) Park, C.; Yoon, J.; Thomas, E. L. *Polymer* **2003**, *44*, 6725−6760.
(4) Black, C. T.; Guarini, K. W.; Zhang, Y.; Kim, H. J.; Benedict, J.; Sikorski, E.; Babich, I. V.; Milkove, K. R. *IEEE Electron Device Lett.* **2004**, *25*, 622−624.
(5) Thurn-Albrecht, T.; Schotter, J.; Kastle, C. A.; Emley, N.; Shibauchi, T.; Krusin-Elbaum, L.; Guarini, K.; Black, C. T.; Tuominen, M. T.; Russell, T. P. *Science* **2000**, *290*, 2126−2129.
(6) Naito, K.; Hieda, H.; Sakurai, M.; Kamata, Y.; Asakawa, K. *IEEE Trans. Magn*. **2002**, *38*, 1949−1951.
(7) Morkved, T. L.; Lu, M.; Urbas, A. M.; Ehrichs, E. E.; Jaeger, H. M.; Mansky, P.; Russell, T. P. *Science* **1996**, *273*, 931−933.
(8) Mansky, P.; DeRouchey, J.; Russell, T. P.; Mays, J.; Pitsikalis, M.; Morkved, T.; Jaeger, H. *Macromolecules* **1998**, *31*, 4399−4401.
(9) Park, C.; De Rosa, C.; Thomas, E. L. *Macromolecules* **2001**, *34*, 2602−2606.
(10) Angelescu, D. E.; Waller, J. H.; Adamson, D. H.; Deshpande, P.; Chou, S. Y.; Register, R. A.; Chaikin, P. M. *Adv. Mater.* **2004**, *16*, 1736−1740.
(11) Segalman, R. A.; Yokoyama, H.; Kramer, E. J. *Adv. Mater* **2001**, *13*, 1152−1155.
(12) Sundrani, D.; Sibener, S. J. *Macromolecules* **2002**, *35*, 8531−8539.
(13) Sundrani, D.; Darling, S. B.; Sibener, S. J. *Langmuir* **2004**, *20*, 5091−5099.
(14) Sundrani, D.; Darling, S. B.; Sibener, S. J. *Nano Lett* **2004**, *4*, 273−276.
(15) Harrison, C.; Dagata, J. A.; Adamson, D. H. In *Developments in Block Copolymer Science and* Technology; Hamley, I. W., Ed.; Wiley: Chichester, 2004; pp 295−323.
(16) Harrison, C.; Adamson, D. H.; Cheng, Z. D.; Sebastian, J. M.; Sethuraman, S.; Huse, D. A.; Register, R. A.; Chaikin, P. M. *Science* **2000**, *290*, 1558−1560.
(17) Harrison, C.; Cheng, Z. D.; Sethuraman, S.; Huse, D. A.; Chaikin, P. M.; Vega, D. A.; Sebastian, J. M.; Register, R. A.; Adamson, D. H. *Phys. Rev. E* **2002**, *66*, 011706.
(18) Angelescu, D. E.; Waller, J. H.; Pelletier, V.; Trawick, M. L.; Register, R. A.; Chaikin, P. M.; Adamson, D. H. *Polym. Prepr.* **2003**, *44*, 226−227.
(19) Interestingly, Morse and Milner have shown that bulk (3D) lamellar block copolymers have no corresponding nematic phase. Although a finite density of small dislocation loops exists in such systems (since these pointlike defects have a finite core and far-field strain energy), they do not interrupt the quasi-long-range order of the layering. Temperatures where significant numbers of unbound dislocation lines would exist (thus creating the nematic phase), however, are above the lamellar−isotropic transition. Morse, D. C.; Milner, S. T. *Phys. Rev. E* **1993**, *47*, 1119−1125.
(20) Man, W.; Angelescu, D. E.; Wu, M. W.; Adamson, D. H.; Register, R. A.; Chaikin, P. M. In *Bulletin of the American Physical Society March Meeting*, Los Angeles, CA, 2005.
(21) Coulon, G.; Ausserre, D.; Russell, T. P. *J. Phys. (Paris)* **1990**, *51*, 777−786.
(22) Russell, T. P.; Coulon, G.; Deline, V. R.; Miller, D. C. *Macromolecules* **1989**, *22*, 4600−4606.
(23) Coulon, G.; Russell, T. P.; Deline, V. R.; Green, P. F. *Macromolecules* **1989**, *22*, 2581−2589.
(24) Segalman, R. A.; Schaefer, K. E.; Fredrickson, G. H.; Kramer, E. J.; Magonov, S. *Macromolecules* **2003**, *36*, 4498−4506.
(25) Segalman, R. A.; Hexemer, A.; Hayward, R. C.; Kramer, E. J. *Macromolecules* **2003**, *36*, 3272−3288.
(26) Freed, K. F. *Adv. Chem. Phys.* **1972**, *22*, 1−128.
(27) Helfand, E.; Tagami, Y. *J. Chem. Phys.* **1972**, *56*, 3592−3601.
(28) Hong, K. M.; Noolandi, J. *Macromolecules* **1981**, *14*, 727−736.
(29) Matsen, M. W.; Schick, M. *Phys. Rev. Lett.* **1994**, *72*, 2660−2663.
(30) Rasmussen, K. O.; Kalosakas, G. *J. Polym. Sci., Polym. Phys.* **2002**, *40*, 1777−1783.
(31) Ceniceros, H. D.; Fredrickson, G. H. *Multiscale Model. Simul*. **2004**, *2*, 452−474.
(32) Tyler, C. A.; Morse, D. C. *Macromolecules* **2003**, *36*, 3764−3774.
(33) Dai, K. H.; Kramer, E. J. *Polymer* **1994**, *35*, 157−161.
(34) Chandrasekhar, S.; Ranganath, G. S. *Adv. Phys.* **1986**, *35*, 507−596.
(35) Pershan, P. S. *J. Appl. Phys.* **1974**, *45*, 1590−1604.
(36) Amundson, K.; Helfand, E. *Macromolecules* **1993**, *26*, 1324−1332.
(37) Netz, R. R.; Andelman, D.; Schick, M. *Phys. Rev. Lett.* **1997**, *79*, 1058−1061.
(38) Matsen, M. W. *J. Chem. Phys.* **1997**, *107*, 8110−8119.
(39) De Gennes, P.-G.; Prost, J. *The Physics of Liquid Crystals*, 2nd ed.; Oxford University Press: Oxford, UK, 1993.
(40) Segalman, R. A.; Hexemer, A.; Kramer, E. J. *Phys. Rev. Lett.* **2003**, *91*, 196101.

MA050479L